Carbazole-Based Hole Transport Polymer for Methylammonium-Free Tin–Lead Perovskite Solar Cells with Enhanced Efficiency and Stability

Jiantao Wang, Zhenhua Yu, Daniel D. Astridge, Zhenyi Ni, Liang Zhao, Bo Chen, Mengru Wang, Ying Zhou, Guang Yang, Xuezeng Dai, Alan Sellinger, and Jinsong Huang*

ABSTRACT: As the most commonly used hole transport material (HTM) in tin–lead (Sn–Pb) perovskite solar cells (PSCs), poly(3,4-ethylenedioxythiophene) polystyrenesulfonate (PEDOT:PSS) limits the power conversion efficiency (PCE) and stability of the PSCs due to its acidic characteristics. Herein, an easily synthesized polymer HTM poly[(phenyl)imino[9-(2-ethylhexyl)carbazole]-2,7-diyl] (CzAn) with a shallow highest occupied molecular orbital (HOMO) level of −4.95 eV is used in a p-i-n structure, methylammonium-free, Sn–Pb PSC to replace PEDOT:PSS. Upon optimization using doping and surface engineering, high quality Sn–Pb PSCs could be successfully fabricated, boosting the PCE to 22.6% (stabilized PCE of 21.3%) compared with 21.2% for PEDOT:PSS. The perovskite films prepared on the modified CzAn HTM possess improved crystallinity, reduced trap-state density, and larger carrier mobility resulting in PSCs with greatly improved stability.

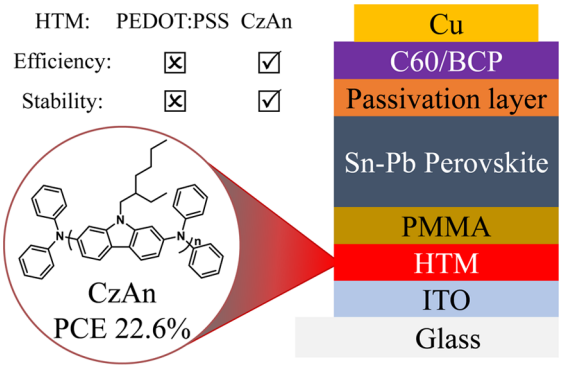

Metal halide perovskites have attracted extensive attention in the optoelectronics community due to their superior properties such as composition-dependent tunable bandgap (E_g), low-cost solution-processing, and rapidly increasing device performance.[1−6] Lead (Pb)-based halide single-junction perovskite solar cells (PSC) have achieved power conversion efficiencies (PCE) over 25%, which makes them a very competitive candidate in next-generation photovoltaic technologies.[7,8] To further improve the PCE close to the Shockley-Queisser efficiency limit, the bandgap of the perovskite absorbers requires narrowing, which is typically achieved by adding tin ions (Sn^{2+}) to replace a portion of the Pb^{2+} ions.[9] Sn–Pb-alloyed perovskites have a lower bandgap of 1.21 eV when the Sn/Pb ratio is ≈1, which is the optimal composition to build perovskite-perovskite tandems.[10] The narrow bandgap Sn–Pb PSCs can be paired with the wide bandgap perovskite to form all-perovskite tandem solar cells, whose PCEs have already been demonstrated to surpass that of the top-performing single-junction PSCs.[11−14] However, one serious concern for Sn–Pb PSCs is their poorer stability than their pure lead-based counterparts.[15]

As the most commonly used HTM in Sn–Pb PSCs, poly(3,4-ethylenedioxythiophene)-poly(styrenesulfonate) (PEDOT:PSS) has advantages of good wetting for reproducible perovskite solution deposition, and appropriate energy levels for efficient hole extraction from Sn–Pb perovskites.[16] However, the PEDOT:PSS HTM accelerates perovskite degradation due to its corrosive acidic characteristics and hygroscopic properties.[17,18] To replace PEDOT:PSS in Sn–Pb PSCs, three classes of HTMs have been investigated: inorganic HTMs, organic small-molecule HTMs, and polymer HTMs. Inorganic HTMs such as nickel oxide (NiO_x) were reported as a promising candidate in Sn–Pb-alloyed PSCs, but the device efficiencies were still lower than those using PEDOT:PSS.[19,20] Recently, Gaurav et al. employed an organic small-molecule-

Received: July 11, 2022
Accepted: September 8, 2022
Published: September 12, 2022

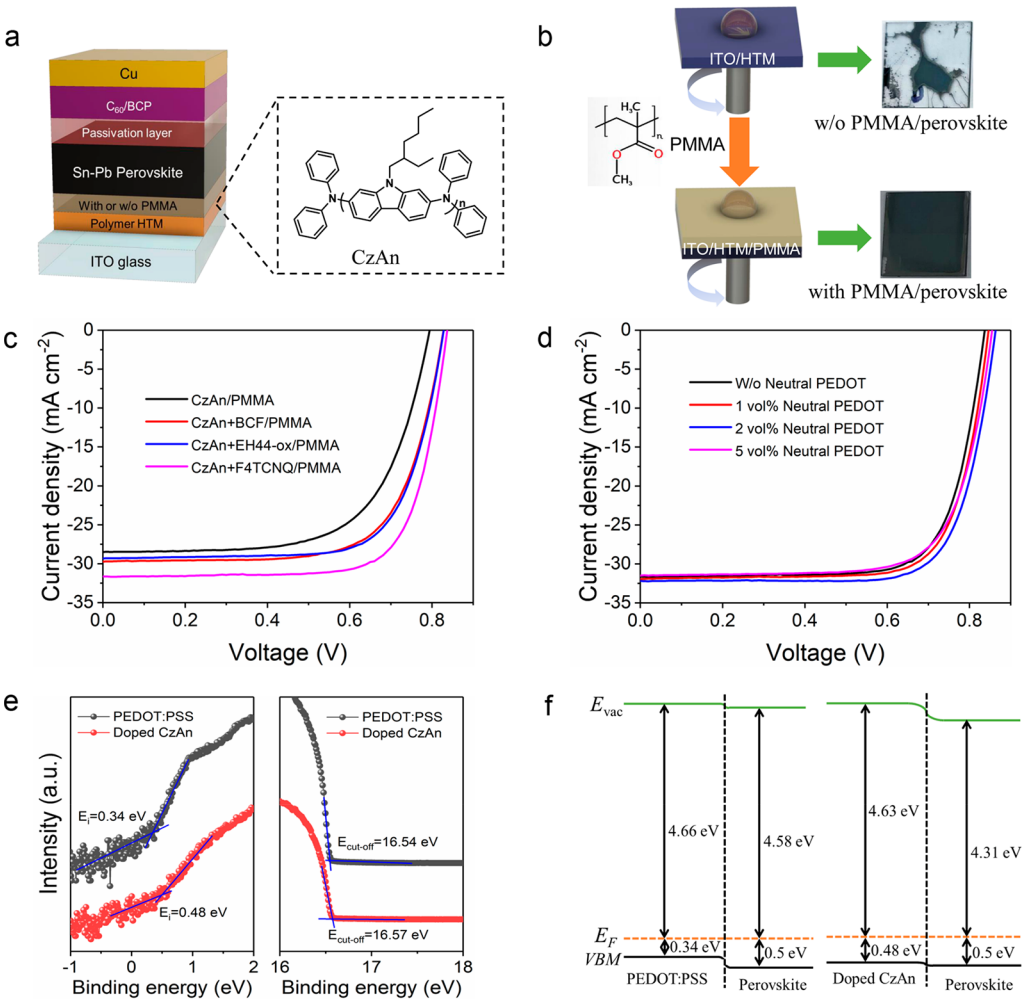

Figure 1. (a) Device structure of Sn−Pb PSCs and molecular structure of CzAn. (b) Images of perovskite coverage on HTM with and without PMMA. (c) Reverse scan current density−voltage (J−V) curves of Sn−Pb PSCs based on CzAn HTM with varying p-type dopants. (d) Different amounts of neutral PEDOT in the CzAn layer. (e) UPS spectra of doped-CzAn and PEDOT:PSS. (f) Energy level alignment of doped-CzAn and PEDOT:PSS with perovskites.

based monolayer as HTM in Sn−Pb PSCs and obtained a higher PCE.[17] However, the sensitive adsorption process of these self-assembled monolayers leads to defects and pinholes in the HTM, that in turn leads to reduced reproducibility of PSCs.[17,21] Polymer HTMs generally have facile processability and better reproducibility, which holds better potential to replace PEDOT:PSS.[22] For instance, poly[bis(4-phenyl)(2,4,6-trimethylphenyl)amine] (PTAA), a widely used HTM in pure Pb PSCs, has achieved an enhanced PCE and thermal stability compared with PEDOT:PSS in Sn−Pb PSCs.[23] However, the mismatched energy levels between PTAA and Sn−Pb perovskites still limits the efficiency of Sn−Pb PSCs. Therefore, it is urgent to find a superior polymer HTM for Sn−Pb PSCs.

In this work, we report a polymer HTM poly[(phenyl)-imino[9-(2-ethylhexyl)carbazole]-2,7-diyl] (CzAn) for use in high efficiency and highly stable methylammonium (MA)-free Sn−Pb PSCs. The CzAn HTM has energy levels well matched for the Sn−Pb layer and when modified with an ultrathin poly(methyl methacrylate) (PMMA) passivation layer, leads to improved wettability to ensure good adhesion of the perovskite layer. A trace amount of 2,3,5,6-tetrafluoro-7,7,8,8-tetracyano-quinodimethane (F4TCNQ) is used as a dopant to enhance the hole conductivity while neutral PEDOT is added to help further tune the energy level of the CzAn HTM. Perovskite films deposited on the modified CzAn show reduced trap-state density and improved carrier transport, that enhances the PSC internal quantum efficiency and current density. Finally, the CzAn-based Sn−Pb PSCs achieved a remarkable PCE of 22.6% (stabilized PCE of 21.3%) with enhanced stability.

Modification process of the CzAn polymer HTM. The device structure and the molecular structure of CzAn are shown in Figure 1a. The methylamine (MA)-free Sn−Pb perovskite has a composition of $FA_{0.8}Cs_{0.2}Sn_{0.5}Pb_{0.5}I_3$ and has shown better stability than volatile-MA embedded perovskites under heat and light.[18,24,25] To further improve the device PCE, a passivation layer was processed on top of the Sn−Pb layer by depositing benzylhydrazine hydrochloride (BHC) and phenyl-C_{61}-butyric acid methyl ester ($PC_{61}BM$) consecutively.[26,27] The fabrication details can be found in the experimental section. CzAn has a highest occupied molecular orbital (HOMO) level of −4.95 eV and a lowest unoccupied molecular orbital (LUMO) level of −2.01 eV,[22] which is comparable with PEDOT:PSS as shown in Figure 1f. The CzAn has a facile synthesis, which can be found in the experimental section, and good thermal stability with a glass

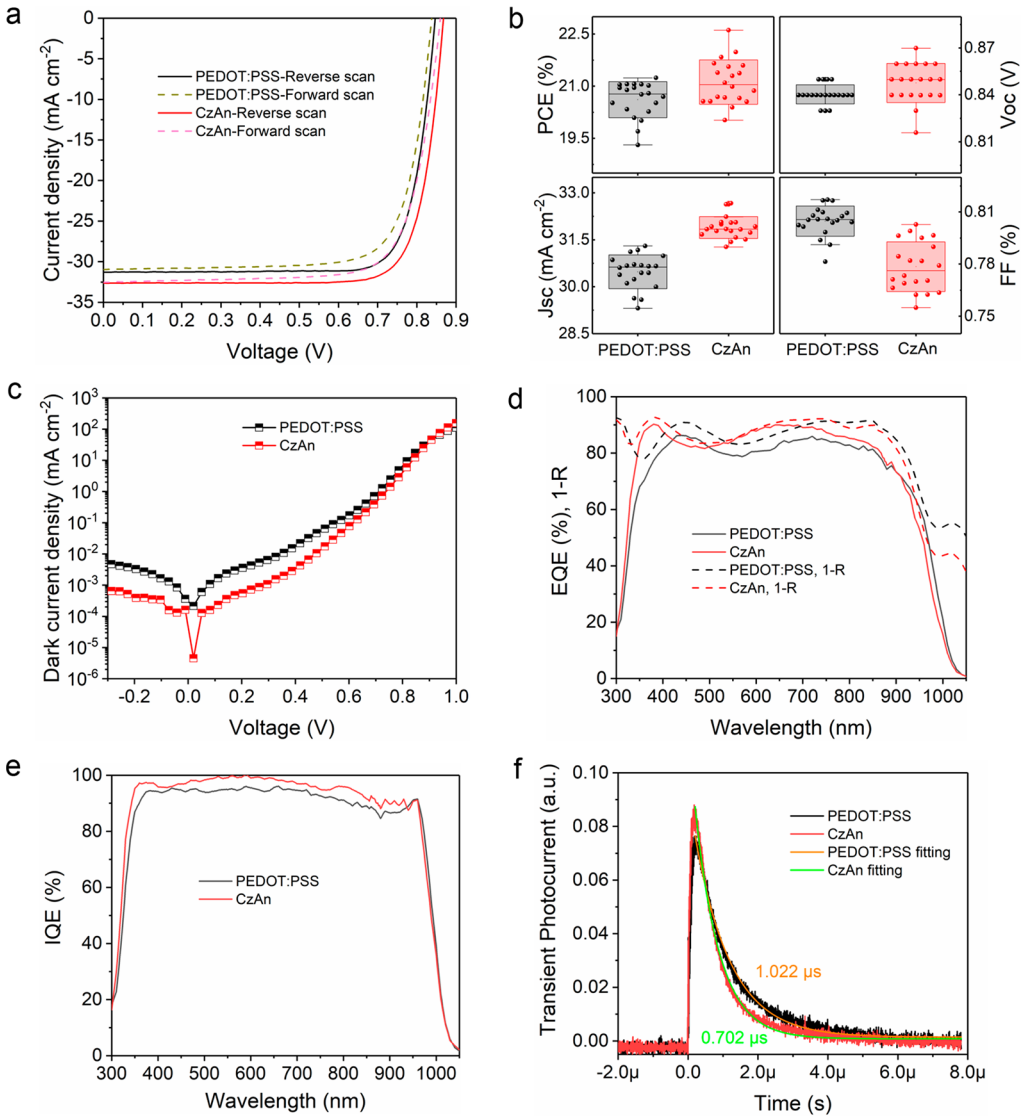

Figure 2. (a) *J*–*V* curves with forward scan and reverse scan of champion devices based on PEDOT:PSS and CzAn. (b) Statistics of PCE, V_{oc}, J_{sc}, and FF of PSCs based on 20 devices. (c) Dark *J*–*V* curves. (d) External quantum efficiency (EQE) and reflected absorption. (e) Internal quantum efficiency (IQE). (f) Transient photocurrent (TPC) of PSCs based on PEDOT:PSS and CzAn HTMs.

transition temperature (T_g) of 146 °C and decomposition temperature (T_d) of 362 °C, making it a promising HTM for Sn–Pb PSCs.[28] This polymer has been applied in p-i-n structured perovskite solar cells to yield an efficiency of 17.2% using $(FA_{0.79}MA_{0.16}Cs_{0.05})Pb(I_{0.84}Br_{0.16})_3$.[22] When we employed CzAn alone in p-i-n structured Sn–Pb PSCs, we found that it was too hydrophobic, leading to discontinuous perovskite thin films, as shown in Figure 1b. To enhance surface hydrophilicity of CzAn, we coated an ultrathin PMMA layer on top, as the carbonyl groups in PMMA enhance wetting with both perovskites and the HTM,[29−31] as shown by the continuous perovskite film coverage in Figure 1b. However, the CzAn/PMMA HTM did not lead to higher efficiency Sn–Pb PSCs, as shown by the photocurrent curves in Figure 1c. We hypothesized that this was caused by the relatively low hole conductivity of CzAn. To test this, we added to the CzAn layer the commonly used p-type dopants 2,3,5,6-tetrafluoro-7,7,8,8-tetracyanoquinodimethane (F4TCNQ), tris(pentafluorophenyl)borane (BCF) and [9-(2-ethylhexyl)-N2,N2,N7,N7-tetrakis(4-methoxyphenyl)-9H-carbazole-2,7-diamine bis(trifluoromethanesulfonyl)imide] (EH44-ox).[28,32,33] All optimized concentrations of the dopants were 1 wt % (wt: weight ratio) relative to CzAn (Figure S1). We measured the energy levels of CzAn with different dopants (pristine, BCF, EH44-ox, and F4-TCNQ) at this optimized concentration using ultraviolet photoelectron spectroscopy (UPS) and observed increased work functions by the dopants (Figure S2), proving the doping effect of these molecules. Among them, F4TCNQ has the best doping effect. As shown in Figure 1c, F4TCNQ doped-CzAn resulted in the best device efficiency. We then optimized the thickness of the F4TCNQ doped-CzAn HTM by tuning the concentration of the precursor solution. As shown in Figure S3, 1 mg mL^{-1} doped-CzAn resulted in the best device efficiency. Though the doped polymer HTM led to high short-circuit current density (J_{sc}) and fill factor (FF), the open-circuit voltage (V_{oc}) was still lower than 0.80 V, which may be due to the slightly mismatched energy level between the Sn–Pb perovskite and HTM. To address this, we added a small amount of neutral PEDOT (HTL Solar 3, Ossila), that is a commercial dispersion

in toluene without the PSS ionomer, to adjust the work function of the F4TCNQ doped-CzAn HTM. We conducted UPS to measure the energy levels of pristine CzAn and CzAn with neutral PEDOT at different concentrations of 1 vol %, 2 vol % and 5 vol % (vol: volume ratio). As shown in Figure S4, the work function of CzAn increased after adding neutral PEDOT. When the concentration of neutral PEDOT is higher than 2 vol %, the work function saturated. Too much neutral PEDOT (5 vol %) might cause aggregation, leading to decreased PCE as shown in Figure 1d. Therefore, 2 vol % neutral PEDOT notably enhanced the V_{oc} to 0.85 V, which is comparable with the device based on PEDOT:PSS HTM. As shown in Figure 1e, the doped-CzAn can have almost the same work function with PEDOT:PSS, and thus can replace acidic PEDOT:PSS to maintain the charge extraction property.

To investigate the impact of PMMA on CzAn, we conducted atomic force microscopy (AFM) under height mode to study the surface morphologies of CzAn with and without PMMA (Figure S5). The coating of CzAn by PMMA resulted in a smoother surface, revealed by the decreased root-mean-square (RMS) roughness from 4.126 to 2.915 nm. We tuned the PMMA coverage by changing its solution concentration, and found it impacted the device performance dramatically. As shown in Figure S6, the optimal concentration of PMMA for the highest device PCE was 0.2 mg mL^{-1}. Raising or lowering the concentration of PMMA relative to the optimal concentration undermined the device performance. This can be explained by the insulating nature of PMMA, in addition to the reported passivation of PMMA to PSCs.[34] Since thick PMMA can block hole transport and lead to more recombination of carriers, while too thin PMMA may not form a continuous layer between perovskite to passivate defects. Using this optimized PMMA thickness (estimated to be 4–8 nm),[35] we obtained the energy levels of perovskites deposited on PEDOT:PSS and doped-CzAn/PMMA, respectively, by UPS measurement, and the results are shown in Figure S7. A schematic diagram of HTMs-perovskites interface is shown in Figure 1f. The work function of perovskite on doped-CzAn/PMMA is lower than on PEDOT:PSS. The deeper HOMO of doped-CzAn matched better with the valence band maximum (VBM) of perovskite. Subsequently, we fabricated Sn–Pb PSCs with the configuration of ITO/polymer HTM/PMMA/Sn–Pb perovskite/passivation layer/C_{60}/BCP/Cu (Figure 1a), in which the polymer HTM refers to the modified CzAn and PEDOT:PSS counterparts.

Device performance and characterization of Sn–Pb PSCs. We measured the device performance by collecting the current density–voltage (J–V) curves with forward and reverse scans of the fabricated devices. The champion devices based on CzAn and PEDOT:PSS are plotted in Figure 2a, and their detailed parameters are listed in Table 1. The CzAn-based devices obtained the highest PCE of 22.6%, with a V_{oc} of 0.87 V, a J_{sc} of 32.6 mA cm^{-2} and an FF of 79.6%, while the optimized devices with PEDOT:PSS HTM had a PCE of 21.2%, a V_{oc} of 0.85 V, a J_{sc} of 31.3 mA cm^{-2} and an FF of 79.8%. We measured the stabilized PCE of the champion devices. The devices showed stabilized efficiencies of 20.1% and 21.3% for PEDOT:PSS and CzAn-based devices, respectively (Figure S8). PMMA was also used in PEDOT:PSS-based devices as a passivation layer but resulted in reduced FF, J_{sc} and PCE compared with the pristine device as shown in Figure S6, so this route was not pursued further. To understand the reproducibility of the HTMs, we fabricated 20 devices for each type of device. The statistical distribution of their PCE, V_{oc}, J_{sc}, and FF are shown in Figure 2b. The calculated mean and standard deviation of V_{oc}, J_{sc}, FF and PCE for CzAn embodied devices are 0.85 ± 0.01 V, 31.89 ± 0.34 mA cm^{-2}, 77.86 ± 0.01% and 21.12 ± 0.62%, respectively. The parameters for PEDOT:PSS-based devices are 0.84 ± 0.01 V, 30.48 ± 0.52 mA cm^{-2}, 80.48 ± 0.01% and 20.62 ± 0.50%, respectively. From these, we conclude that the PCE increase of the devices with the modified CzAn HTM comes from the enhancement of V_{oc} and J_{sc}, despite a small decrease in FF likely caused by insulating PMMA.[30]

Table 1. Photovoltaic Performance Parameters of the Champion Devices with PEDOT:PSS and CzAn as an HTM

Devices	Scan direction	V_{oc} [V]	J_{sc} [mA cm^{-2}]	FF [%]	PCE [%]
PEDOT:PSS	Forward scan	0.82	30.99	78.07	19.84
	Reverse scan	0.85	31.31	79.81	21.24
CzAn	Forward scan	0.82	32.54	79.26	21.15
	Reverse scan	0.87	32.64	79.62	22.61

We conducted device characterization to understand why CzAn enhances the device performance. To analyze the V_{oc} of the devices, we collected the J–V curves under dark conditions. As shown in Figure 2c, the leakage current density of the PEDOT:PSS-based device is 10 times larger than the CzAn-based device, The smaller dark current density of CzAn-based device agrees with the increase of V_{oc}.[36] The reduced trap density of states (tDOS) in the CzAn-based device was further demonstrated by the thermal admittance spectroscopy (TAS) results displayed in Figure S9. TAS is an established method that can quantitatively compare the trap density of states in the profiling energy depth.[37,38] Two shallow trap bands (0.3–0.35 eV and 0.35–0.48 eV) and one deeper trap band (>0.48 eV) were found in the Sn–Pb PSCs. The tDOS of PEDOT:PSS-based PSCs in the entire trap depth is higher, which indicates the existence of abundant surface and bulk defects that result in lower V_{oc}.

To analyze the increase of the J_{sc}, we measured the external quantum efficiency (EQE) curves of the champion devices with CzAn and PEDOT:PSS HTMs. As shown in Figure 2d, the EQE of the CzAn-based device is higher than that using PEDOT:PSS in the wavelength range of 300–950 nm. The J_{sc} integrated from the EQE curve for the CzAn-based device is 31.2 mA cm^{-2}, 3% higher than that based on PEDOT:PSS (30.2 mA cm^{-2}), which agrees with J–V curves. We observed that the EQE peaks shifted for the two types of devices, which could be caused by the different optical interference. To examine what is the actual charge collection efficiency, the internal quantum efficiency needs to be derived. To that end, we compared their optical losses by measuring the device reflectance. The absorption in the devices at each wavelength can be derived from 100% − reflectance (R) by assuming other parasitic absorption is negligible. The dashed lines in Figure 2d show the absorption curves calculated from the reflection spectra of the two types of devices measured using a spectrometer with an integration sphere. The actual absorption curves have the same trend with the corresponding EQE curves, that confirms that the shape change of EQE curves is primarily derived from the interference. We further obtained the internal quantum efficiency (IQE) spectra using EQE and $(1 - R)$:

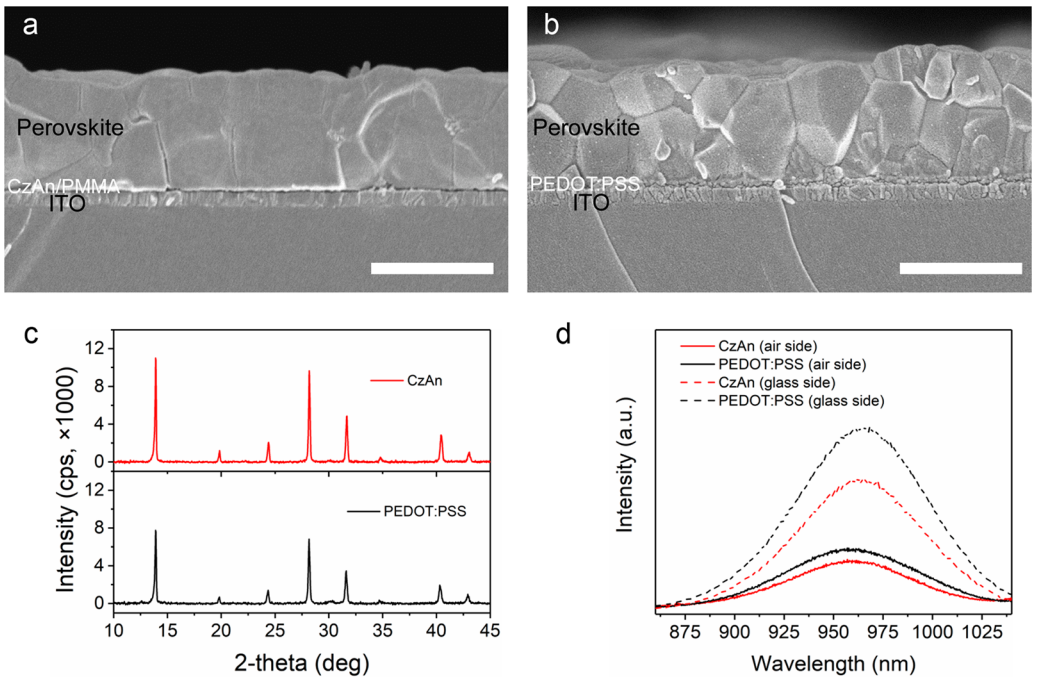

Figure 3. Cross section morphology of perovskite deposited on (a) ITO/CzAn and (b) ITO/PEDOT:PSS; scale bar is 1 μm. (c) XRD patterns of perovskite films. The cps stands for counts per second. (d) PL of perovskite films deposited on ITO/CzAn and ITO/PEDOT:PSS. Perovskite surfaces were covered with a layer of perfluoro(1-butenyl vinyl ether) polymer (CYTOP) before the PL measurements.

$$\mathrm{IQE} = \mathrm{EQE}/(1 - R) \quad (1)$$

As shown in Figure 2e, the IQE of CzAn-based device displayed an overall enhancement in the absorption spectrum range of 300−950 nm. We analyzed the carrier transport across the device by performing the transient photocurrent (TPC) measurements.[39] The photocurrent produced a transient voltage signal on a 50 Ω resistor, that was recorded by an oscilloscope. As shown in Figure 2f, the transient time (τ) in CzAn-based PSCs is 0.702 μs, shorter than that in PEDOT:PSS devices (1.022 μs). Even though the film thicknesses (L) of the perovskite layers are different, as shown in Figure S12, the larger diffusivity of the CzAn-based device (D, $D = L^2/\tau$) mainly comes from a smaller τ. It reveals that the Sn−Pb perovskites grown on modified CzAn have an enhanced carrier transport capacity, that increases J_{sc}.[40] We have studied the trap density in perovskites and found that Sn−Pb perovskites grown on modified CzAn had smaller trap-state density, as shown in Figure S9, that explains the better mobility.

Characterizations of perovskite films. To study the origin of the better-quality Sn−Pb perovskites grown on modified CzAn, we studied the morphology and crystallinity using scanning electron microscopy (SEM) and XRD. As shown in Figure S10, Sn−Pb perovskite films are dense and pinhole free. Some chemical residuals remained at the grain boundaries of the Sn−Pb perovskite on the modified CzAn, which might be assigned as SnF_2 additives that was added to precipitate oxidized Sn^{2+}.[41−43] Their cross-sectional SEM images are shown in Figure 3a,b. Perovskite films deposited on CzAn are relatively flat with smoother top and bottom surfaces, that is beneficial to form more intimate contacts with both sides. In contrast, perovskite film on PEDOT:PSS has obvious grain delamination with higher undulation on the top surface and fine grains at the bottom contact, which could allow for more recombination centers. As shown in Figure 3c, the intensity of XRD patterns of perovskite on CzAn/PMMA is higher than that on PEDOT:PSS. The full width at half-maximum (FWHM) values at the typical perovskite characteristic peak of 13.92° are 0.1002° and 0.1258° for CzAn and PEDOT:PSS-based samples, respectively. A higher XRD peak intensity for CzAn-based perovskite film with smaller FWHM indicates a better film crystallinity, that explains the lower trap density in these perovskites.

To gain more insight on the optoelectronic properties of the perovskite deposited on the modified CzAn and PEDOT:PSS, we measured their UV−vis−NIR absorption and photoluminescence (PL). As shown in Figure S11, both films have no obvious change of optical bandgap of 1.22 eV, but surprisingly the absorption of the Sn−Pb perovskite film on PEDOT:PSS is slightly stronger than that on modified CzAn. The measured Sn−Pb perovskite film thicknesses are 916.09 and 966.41 nm for the films deposited on modified CzAn and PEDOT:PSS, respectively (Figure S12), explaining the reduced absorption. This also explains the observed difference of interference in the devices and thus changed EQE shapes. On the other hand, it suggests decreased recombination and enhanced charge collection in the thinner perovskite film on the modified CzAn as it had a higher J_{sc} despite weaker light absorption. We performed PL experiments of perovskite films on the half device stack of ITO/modified CzAn/perovskite and ITO/PEDOT:PSS/perovskite. As shown in Figure 3d, the CzAn-based perovskite film has lower PL intensity no matter if the incident light came from the air side or glass side. As we have confirmed the deep charge trap density in the CzAn-based perovskite film is lower, which corresponds to less trap-assisted recombination, the reduced PL emission can be explained by enhanced hole extraction to the HTM and then ITO.

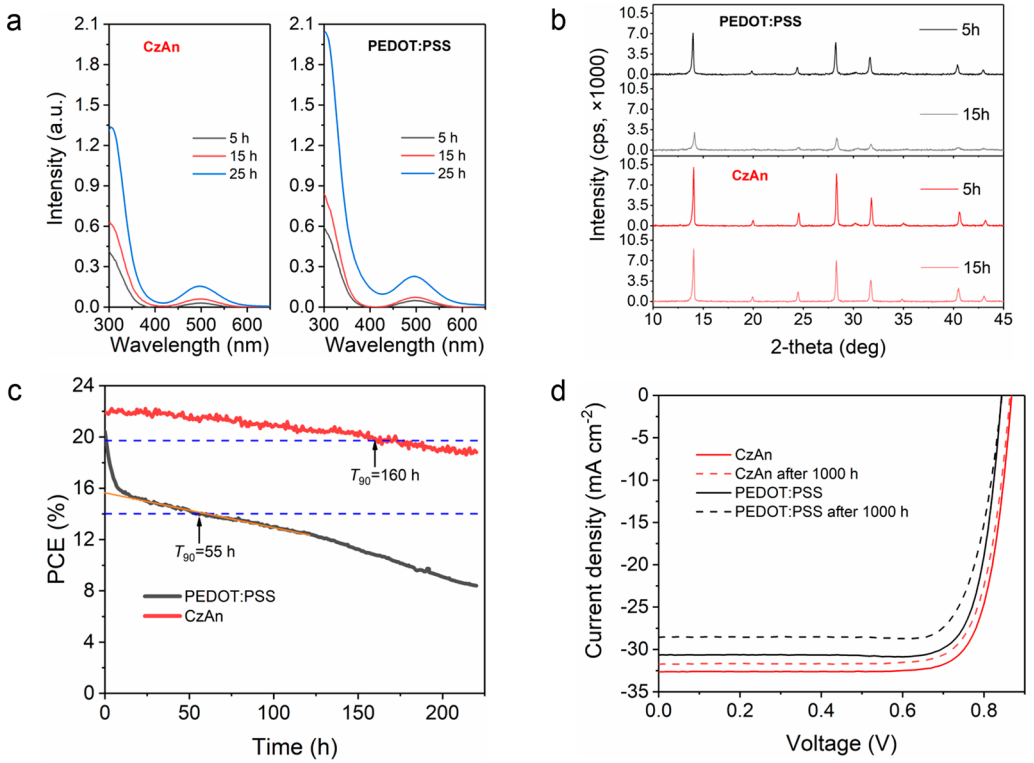

Figure 4. (a) Absorption spectra of the toluene, in which perovskite films deposited on CzAn/PMMA or PEDOT:PSS were immersed under 1 sun illumination for 5, 15, and 25 h. (b) XRD patterns of perovskite films deposited on CzAn/PMMA or PEDOT:PSS and immersed in toluene under 1 sun illumination for 5 and 15 h. (c) Maximum power point (MPP) output of the devices based on PEDOT:PSS and CzAn. (d) *J*–*V* curves of Sn–Pb-alloyed PSCs based on CzAn and PEDOT:PSS before and after storing for 1000 h.

Stability measurements of perovskite films and devices. To examine how the changed film quality affects the light stability of Sn–Pb perovskites, we studied the light generation of iodine (I_2) in these films, as it was reported to be the main reason for the rapid degradation of fully encapsulated perovskites.[44] Perovskite films deposited on modified CzAn or PEDOT:PSS were immersed into toluene to extract I_2 generated in films, as shown in Figure S13. By measuring the absorption spectra of the two toluene solutions after light soaking for different durations, the I_2 generation rate can be directly compared.[45,46] According to the absorption spectra as shown in Figure 4a, the I_2 generation rate in the Sn–Pb perovskite on modified CzAn is slower than that on PEDOT:PSS, that indicates the improved crystallinity helps stabilize Sn–Pb perovskites under illumination. We removed the films after light soaking for 5 and 15 h and performed XRD on the films. The XRD peak intensities decreased over time (Figure 4b). The FWHM of the XRD peak at 13.92° increased to 0.1759° and 0.1277° relative to the initial measurements in Figure 3c for films on PEDOT:PSS and CzAn, respectively, after 15 h light soaking. The rate of degradation of the perovskite film on PEDOT:PSS is faster in terms of the more rapid increase of FWHM, that agree with the I_2 extracted into toluene data. The slower degradation of CzAn than PEDOT:PSS can be explained by the much faster degradation of Sn–Pb perovskites induced by acidic PEDOT:PSS. The dopant of F4-TCNQ and neutral PEDOT improves the stability of Sn–Pb perovskites by matching the energy levels of new HTM with Sn–Pb perovskites. PMMA contributes by surface energy modification to enable the coating of smooth and highly crystalline Sn–Pb perovskite films, in addition to its defect passivation function.

To study the stability of photovoltaic devices, we measured the maximum power point (MPP) outputs under 1 sun illumination without cooling. As shown in Figure 4c, the PEDOT:PSS-based device presents obvious burn-in effect with a rapid PCE decrease in the first 10 h, which may be due to the instability at PEDOT:PSS/perovskite interface.[47] For long-term photostability tracking, the CzAn-based device can maintain 90% of the initial PCE (T_{90}) for 160 h while PEDOT:PSS only kept T_{90} for 55 h. Moreover, the shelf life stability of encapsulated devices under ambient conditions was studied by measuring the device *J*–*V* curves. The CzAn-based device retained 96% of the initial PCE after 1000 h storage while that for the PEDOT:PSS-based device decreased to 91% (Figure S14). We plotted their *J*–*V* curves at 0 and 1000 h in Figure 4d. Even after 1000 h, the resultant PCE of 21.65% for CzAn-based device is still higher than the initial PCE of 21.02% for PEDOT:PSS-based device, as listed in Table S1.

In conclusion, we reported a modified CzAn polymer as HTM in Sn–Pb PSCs to obtain a remarkable PCE of 22.6% (stabilized PCE of 21.3%) with enhanced stability. After modifying CzAn by doping and surface engineering, high quality Sn–Pb perovskites could be fabricated. Perovskite films deposited on the modified HTM showed improved crystallization, reduced trap-state density and better charge collection efficiency. Better film quality of perovskite deposited on the modified HTM compared with PEDOT:PSS contributed to an overall increase of the internal quantum efficiency and the enhanced photocurrent density to 32.6 mA cm^{-2}. Finally, Sn–Pb PSCs using CzAn HTM shows improved stability over PEDOT:PSS from reduced I_2 generation under light exposure, MPP, and after 1000 h encapsulated device storage. This work

paves a way for utilizing custom prepared hole transport polymers to fabricate Sn−Pb PSCs with high-performance and it holds promise to further enhance the PCE and stability of integrated all-perovskite tandem solar cells.

■ ASSOCIATED CONTENT

Supporting Information

The Supporting Information is available free of charge at https://pubs.acs.org/doi/10.1021/acsenergylett.2c01578.

Experimental methods, optimization of CzAn concentrations, UPS spectra, AFM morphologies, optimization of PMMA concentrations, tDOS, SEM surface morphologies, UV−vis−NIR absorption of perovskite films, thickness profiles, experimental setup of film stability measurements, storage stability tracking, and photovoltaic parameters of PSCs before and after 1000 h (PDF)

■ AUTHOR INFORMATION

Corresponding Author

Jinsong Huang − *Department of Applied Physical Sciences and Department of Chemistry, University of North Carolina at Chapel Hill, Chapel Hill, North Carolina 27599, United States;* orcid.org/0000-0002-0509-8778; Email: jhuang@unc.edu

Authors

Jiantao Wang − *Department of Applied Physical Sciences, University of North Carolina at Chapel Hill, Chapel Hill, North Carolina 27599, United States;* orcid.org/0000-0002-1929-3339

Zhenhua Yu − *Department of Applied Physical Sciences, University of North Carolina at Chapel Hill, Chapel Hill, North Carolina 27599, United States*

Daniel D. Astridge − *Department of Chemistry, Colorado School of Mines, Golden, Colorado 80401, United States;* orcid.org/0000-0002-8504-260X

Zhenyi Ni − *Department of Applied Physical Sciences, University of North Carolina at Chapel Hill, Chapel Hill, North Carolina 27599, United States;* orcid.org/0000-0002-8379-9182

Liang Zhao − *Department of Applied Physical Sciences, University of North Carolina at Chapel Hill, Chapel Hill, North Carolina 27599, United States*

Bo Chen − *Department of Applied Physical Sciences, University of North Carolina at Chapel Hill, Chapel Hill, North Carolina 27599, United States*

Mengru Wang − *Department of Applied Physical Sciences, University of North Carolina at Chapel Hill, Chapel Hill, North Carolina 27599, United States;* orcid.org/0000-0003-1864-2207

Ying Zhou − *Department of Applied Physical Sciences, University of North Carolina at Chapel Hill, Chapel Hill, North Carolina 27599, United States*

Guang Yang − *Department of Applied Physical Sciences, University of North Carolina at Chapel Hill, Chapel Hill, North Carolina 27599, United States*

Xuezeng Dai − *Department of Applied Physical Sciences, University of North Carolina at Chapel Hill, Chapel Hill, North Carolina 27599, United States;* orcid.org/0000-0002-5544-590X

Alan Sellinger − *Department of Chemistry and Department of Materials Science, Colorado School of Mines, Golden, Colorado 80401, United States; National Renewable Energy Laboratory, Golden, Colorado 80401, United States;* orcid.org/0000-0001-6705-1548

Complete contact information is available at: https://pubs.acs.org/10.1021/acsenergylett.2c01578

Author Contributions

J.W. and Z.Y. contributed to this work equally.

Notes

The authors declare no competing financial interest.

■ ACKNOWLEDGMENTS

This work is mainly supported by the U.S. Department of Energy, Office of Energy Efficiency and Renewable Energy, Solar Energy Technologies Office by Award Number DE-EE0008749. D.D.A. acknowledges the Department of Chemistry at the Colorado School of Mines for providing Teaching Assistantships during the course of this research. This work was partially supported by the U.S. Department of Energy, Office of Energy Efficiency and Renewable Energy, Solar Energy Technologies Office by Award Number DE-EE0008978.

■ REFERENCES

(1) Kojima, A.; Teshima, K.; Shirai, Y.; Miyasaka, T. Organometal Halide Perovskites as Visible-Light Sensitizers for Photovoltaic Cells. *Journal of The American Chemical Society* **2009**, *131*, 6050−6051.

(2) Lee, M. M.; Teuscher, J.; Miyasaka, T.; Murakami, T. N.; Snaith, H. J. Efficient Hybrid Solar Cells Based on Meso-Superstructured Organometal Halide Perovskites. *Science* **2012**, *338*, 643−647.

(3) Kim, H. S.; Lee, C. R.; Im, J. H.; Lee, K. B.; Moehl, T.; Marchioro, A.; Moon, S. J.; Humphry-Baker, R.; Yum, J. H.; Moser, J. E.; Gratzel, M.; Park, N. G. Lead iodide perovskite sensitized all-solid-state submicron thin film mesoscopic solar cell with efficiency exceeding 9%. *Sci. Rep* **2012**, *2*, 591.

(4) Jeon, N. J.; Noh, J. H.; Kim, Y. C.; Yang, W. S.; Ryu, S.; Seok, S. I. Solvent engineering for high-performance inorganic-organic hybrid perovskite solar cells. *Nat. Mater.* **2014**, *13*, 897−903.

(5) Yang, W. S.; Noh, J. H.; Jeon, N. J.; Kim, Y. C.; Ryu, S.; Seo, J.; Seok, S. I. High-performance photovoltaic perovskite layers fabricated through intramolecular exchange. *Science* **2015**, *348*, 1234−1237.

(6) Eperon, G. E.; Leijtens, T.; Bush, K. A.; Prasanna, R.; Green, T.; Wang, J. T.-W.; McMeekin, D. P.; Volonakis, G.; Milot, R. L.; May, R.; Palmstrom, A.; Slotcavage, D. J.; Belisle, R. A.; Patel, J. B.; Parrott, E. S.; Sutton, R. J.; Ma, W.; Moghadam, F.; Conings, B.; Babayigit, A.; Boyen, H.-G.; Bent, S.; Giustino, F.; Herz, L. M.; Johnston, M. B.; McGehee, M. D.; Snaith, H. J. Perovskite-perovskite tandem photovoltaics with optimized band gaps. *Science* **2016**, *354*, 861−865.

(7) Min, H.; Lee, D. Y.; Kim, J.; Kim, G.; Lee, K. S.; Kim, J.; Paik, M. J.; Kim, Y. K.; Kim, K. S.; Kim, M. G.; Shin, T. J.; Il Seok, S. Perovskite solar cells with atomically coherent interlayers on SnO2 electrodes. *Nature* **2021**, *598*, 444−450.

(8) Kim, M.; Jeong, J.; Lu, H.; Lee, T. K.; Eickemeyer, F. T.; Liu, Y.; Choi, I. W.; Choi, S. J.; Jo, Y.; Kim, H.-B.; Mo, S.-I.; Kim, Y.-K.; Lee, H.; An, N. G.; Cho, S.; Tress, W. R.; Zakeeruddin, S. M.; Hagfeldt, A.; Kim, J. Y.; Grätzel, M.; Kim, D. S. Conformal quantum dot−SnO2 layers as electron transporters for efficient perovskite solar cells. *Science* **2022**, *375*, 302−306.

(9) Cao, J.; Loi, H. L.; Xu, Y.; Guo, X.; Wang, N.; Liu, C. K.; Wang, T.; Cheng, H.; Zhu, Y.; Li, M. G.; Wong, W. Y.; Yan, F. High-Performance Tin-Lead Mixed-Perovskite Solar Cells with Vertical Compositional Gradient. *Adv. Mater.* **2022**, *34*, 2107729.

(10) Rajagopal, A.; Yang, Z.; Jo, S. B.; Braly, I. L.; Liang, P. W.; Hillhouse, H. W.; Jen, A. K. Highly Efficient Perovskite-Perovskite

Tandem Solar Cells Reaching 80% of the Theoretical Limit in Photovoltage. *Adv. Mater.* **2017**, *29*, 1702140.
(11) Yu, Z. H.; Yang, Z. B.; Ni, Z. Y.; Shao, Y. C.; Chen, B.; Lin, Y. Z.; Wei, H. T.; Yu, Z. S. J.; Holman, Z.; Huang, J. S. Simplified interconnection structure based on C-60/SnO(2-x)for all-perovskite tandem solar cells. *Nat. Energy* **2020**, *5*, 657−665.
(12) Lin, R.; Xu, J.; Wei, M.; Wang, Y.; Qin, Z.; Liu, Z.; Wu, J.; Xiao, K.; Chen, B.; Park, S. M.; Chen, G.; Atapattu, H. R.; Graham, K. R.; Xu, J.; Zhu, J.; Li, L.; Zhang, C.; Sargent, E. H.; Tan, H. All-perovskite tandem solar cells with improved grain surface passivation. *Nature* **2022**, *603*, 73−78.
(13) Yu, Z.; Chen, X.; Harvey, S. P.; Ni, Z.; Chen, B.; Chen, S.; Yao, C.; Xiao, X.; Xu, S.; Yang, G.; Yan, Y.; Berry, J. J.; Beard, M. C.; Huang, J. Gradient Doping in Sn-Pb Perovskites by Barium Ions for Efficient Single-junction and Tandem Solar Cells. *Adv. Mater.* **2022**, *34*, 2110351.
(14) Li, L.; Wang, Y.; Wang, X.; Lin, R.; Luo, X.; Liu, Z.; Zhou, K.; Xiong, S.; Bao, Q.; Chen, G.; Tian, Y.; Deng, Y.; Xiao, K.; Wu, J.; Saidaminov, M. I.; Lin, H.; Ma, C.-Q.; Zhao, Z.; Wu, Y.; Zhang, L.; Tan, H. Flexible all-perovskite tandem solar cells approaching 25% efficiency with molecule-bridged hole-selective contact. *Nat. Energy* **2022**, *7*, 708.
(15) Tong, J.; Jiang, Q.; Ferguson, A. J.; Palmstrom, A. F.; Wang, X.; Hao, J.; Dunfield, S. P.; Louks, A. E.; Harvey, S. P.; Li, C.; Lu, H.; France, R. M.; Johnson, S. A.; Zhang, F.; Yang, M.; Geisz, J. F.; McGehee, M. D.; Beard, M. C.; Yan, Y.; Kuciauskas, D.; Berry, J. J.; Zhu, K. Carrier control in Sn−Pb perovskites via 2D cation engineering for all-perovskite tandem solar cells with improved efficiency and stability. *Nat. Energy* **2022**, *7*, 642.
(16) Chin, Y.-C.; Daboczi, M.; Henderson, C.; Luke, J.; Kim, J.-S. Suppressing PEDOT:PSS Doping-Induced Interfacial Recombination Loss in Perovskite Solar Cells. *Acs Energy Lett.* **2022**, *7*, 560−568.
(17) Kapil, G.; Bessho, T.; Sanehira, Y.; Sahamir, S. R.; Chen, M.; Baranwal, A. K.; Liu, D.; Sono, Y.; Hirotani, D.; Nomura, D.; Nishimura, K.; Kamarudin, M. A.; Shen, Q.; Segawa, H.; Hayase, S. Tin−Lead Perovskite Solar Cells Fabricated on Hole Selective Monolayers. *Acs Energy Lett.* **2022**, *7*, 966−974.
(18) Prasanna, R.; Leijtens, T.; Dunfield, S. P.; Raiford, J. A.; Wolf, E. J.; Swifter, S. A.; Werner, J.; Eperon, G. E.; de Paula, C.; Palmstrom, A. F.; Boyd, C. C.; van Hest, M. F. A. M.; Bent, S. F.; Teeter, G.; Berry, J. J.; McGehee, M. D. Design of low bandgap tin-lead halide perovskite solar cells to achieve thermal, atmospheric and operational stability. *Nat. Energy* **2019**, *4*, 939−947.
(19) Han, Q.; Wei, Y.; Lin, R.; Fang, Z.; Xiao, K.; Luo, X.; Gu, S.; Zhu, J.; Ding, L.; Tan, H. Low-temperature processed inorganic hole transport layer for efficient and stable mixed Pb-Sn low-bandgap perovskite solar cells. *Science Bulletin* **2019**, *64*, 1399−1401.
(20) Gao, H.; Lu, Q.; Xiao, K.; Han, Q.; Lin, R.; Liu, Z.; Li, H.; Li, L.; Luo, X.; Gao, Y.; Wang, Y.; Wen, J.; Zou, Z.; Zhou, Y.; Tan, H. Thermally Stable All-Perovskite Tandem Solar Cells Fully Using Metal Oxide Charge Transport Layers and Tunnel Junction. *Sol Rrl* **2021**, *5*, 2100814.
(21) Sun, J.; Shou, C.; Sun, J.; Wang, X.; Yang, Z.; Chen, Y.; Wu, J.; Yang, W.; Long, H.; Ying, Z.; Yang, X.; Sheng, J.; Yan, B.; Ye, J. NiOx-Seeded Self-Assembled Monolayers as Highly Hole-Selective Passivating Contacts for Efficient Inverted Perovskite Solar Cells. *Sol Rrl* **2021**, *5*, 2100663.
(22) Astridge, D. D.; Hoffman, J. B.; Zhang, F.; Park, S. Y.; Zhu, K.; Sellinger, A. Polymer Hole Transport Materials for Perovskite Solar Cells via Buchwald−Hartwig Amination. *ACS Applied Polymer Materials* **2021**, *3*, 5578−5587.
(23) Werner, J.; Moot, T.; Gossett, T. A.; Gould, I. E.; Palmstrom, A. F.; Wolf, E. J.; Boyd, C. C.; van Hest, M. F. A. M.; Luther, J. M.; Berry, J. J.; McGehee, M. D. Improving Low-Bandgap Tin-Lead Perovskite Solar Cells via Contact Engineering and Gas Quench Processing. *Acs Energy Lett.* **2020**, *5*, 1215−1223.
(24) Tong, J.; Gong, J.; Hu, M.; Yadavalli, S. K.; Dai, Z.; Zhang, F.; Xiao, C.; Hao, J.; Yang, M.; Anderson, M. A.; Ratcliff, E. L.; Berry, J. J.; Padture, N. P.; Zhou, Y.; Zhu, K. High-performance methylammonium-free ideal-band-gap perovskite solar cells. *Matter* **2021**, *4*, 1365−1376.
(25) Li, C.; Song, Z.; Chen, C.; Xiao, C.; Subedi, B.; Harvey, S. P.; Shrestha, N.; Subedi, K. K.; Chen, L.; Liu, D.; Li, Y.; Kim, Y.-W.; Jiang, C.-s.; Heben, M. J.; Zhao, D.; Ellingson, R. J.; Podraza, N. J.; Al-Jassim, M.; Yan, Y. Low-bandgap mixed tin−lead iodide perovskites with reduced methylammonium for simultaneous enhancement of solar cell efficiency and stability. *Nat. Energy* **2020**, *5*, 768−776.
(26) Warby, J.; Zu, F.; Zeiske, S.; Gutierrez-Partida, E.; Frohloff, L.; Kahmann, S.; Frohna, K.; Mosconi, E.; Radicchi, E.; Lang, F.; Shah, S.; Peña-Camargo, F.; Hempel, H.; Unold, T.; Koch, N.; Armin, A.; De Angelis, F.; Stranks, S. D.; Neher, D.; Stolterfoht, M. Understanding Performance Limiting Interfacial Recombination in pin Perovskite Solar Cells. *Adv. Energy Mater.* **2022**, *12*, 2103567.
(27) Chen, S.; Xiao, X.; Gu, H.; Huang, J. Iodine reduction for reproducible and high-performance perovskite solar cells and modules. *Sci. Adv.* **2021**, *7*, eabe8130.
(28) Schloemer, T. H.; Gehan, T. S.; Christians, J. A.; Mitchell, D. G.; Dixon, A.; Li, Z.; Zhu, K.; Berry, J. J.; Luther, J. M.; Sellinger, A. Thermally Stable Perovskite Solar Cells by Systematic Molecular Design of the Hole-Transport Layer. *Acs Energy Lett.* **2019**, *4*, 473−482.
(29) Peng, J.; Khan, J. I.; Liu, W.; Ugur, E.; Duong, T.; Wu, Y.; Shen, H.; Wang, K.; Dang, H.; Aydin, E.; Yang, X.; Wan, Y.; Weber, K. J.; Catchpole, K. R.; Laquai, F.; Wolf, S.; White, T. P. A Universal Double-Side Passivation for High Open-Circuit Voltage in Perovskite Solar Cells: Role of Carbonyl Groups in Poly(methyl methacrylate). *Adv. Energy Mater.* **2018**, *8*, 1801208.
(30) Peng, J.; Walter, D.; Ren, Y.; Tebyetekerwa, M.; Wu, Y.; Duong, T.; Lin, Q.; Li, J.; Lu, T.; Mahmud, M. A.; Lem, O. L. C.; Zhao, S.; Liu, W.; Liu, Y.; Shen, H.; Li, L.; Kremer, F.; Nguyen, H. T.; Choi, D.-Y.; Weber, K. J.; Catchpole, K. R.; White, T. P. Nanoscale localized contacts for high fill factors in polymer-passivated perovskite solar cells. *Science* **2021**, *371*, 390−395.
(31) Peng, J.; Kremer, F.; Walter, D.; Wu, Y.; Ji, Y.; Xiang, J.; Liu, W.; Duong, T.; Shen, H.; Lu, T.; Brink, F.; Zhong, D.; Li, L.; Lee Cheong Lem, O.; Liu, Y.; Weber, K. J.; White, T. P.; Catchpole, K. R. Centimetre-scale perovskite solar cells with fill factors of more than 86%. *Nature* **2022**, *601*, 573−578.
(32) Wang, Q.; Bi, C.; Huang, J. S. Doped hole transport layer for efficiency enhancement in planar heterojunction organolead trihalide perovskite solar cells. *Nano Energy* **2015**, *15*, 275−280.
(33) Zhao, Y.; Heumueller, T.; Zhang, J.; Luo, J.; Kasian, O.; Langner, S.; Kupfer, C.; Liu, B.; Zhong, Y.; Elia, J.; Osvet, A.; Wu, J.; Liu, C.; Wan, Z.; Jia, C.; Li, N.; Hauch, J.; Brabec, C. J. A bilayer conducting polymer structure for planar perovskite solar cells with over 1,400 h operational stability at elevated temperatures. *Nat. Energy* **2022**, *7*, 144−152.
(34) Ochoa-Martinez, E.; Ochoa, M.; Ortuso, R. D.; Ferdowsi, P.; Carron, R.; Tiwari, A. N.; Steiner, U.; Saliba, M. Physical Passivation of Grain Boundaries and Defects in Perovskite Solar Cells by an Isolating Thin Polymer. *Acs Energy Lett.* **2021**, *6*, 2626−2634.
(35) Wang, J.; Xu, J.; Li, Z.; Lin, X.; Yu, C.; Wu, H.; Wang, H.-l. Front-Contact Passivation of PIN MAPbI3 Solar Cells with Superior Device Performances. *ACS Applied Energy Materials* **2020**, *3*, 6344−6351.
(36) Li, C.; Song, Z.; Zhao, D.; Xiao, C.; Subedi, B.; Shrestha, N.; Junda, M. M.; Wang, C.; Jiang, C. S.; Al-Jassim, M.; Ellingson, R. J.; Podraza, N. J.; Zhu, K.; Yan, Y. Reducing Saturation-Current Density to Realize High-Efficiency Low-Bandgap Mixed Tin−Lead Halide Perovskite Solar Cells. *Adv. Energy Mater.* **2019**, *9*, 1803135.
(37) Wang, Q.; Shao, Y. C.; Dong, Q. F.; Xiao, Z. G.; Yuan, Y. B.; Huang, J. S. Large fill-factor bilayer iodine perovskite solar cells fabricated by a low-temperature solution-process. *Energ Environ. Sci.* **2014**, *7*, 2359−2365.
(38) Shao, Y.; Xiao, Z.; Bi, C.; Yuan, Y.; Huang, J. Origin and elimination of photocurrent hysteresis by fullerene passivation in CH3NH3PbI3 planar heterojunction solar cells. *Nat. Commun.* **2014**, *5*, 5784.

(39) Zhu, C.; Niu, X.; Fu, Y.; Li, N.; Hu, C.; Chen, Y.; He, X.; Na, G.; Liu, P.; Zai, H.; Ge, Y.; Lu, Y.; Ke, X.; Bai, Y.; Yang, S.; Chen, P.; Li, Y.; Sui, M.; Zhang, L.; Zhou, H.; Chen, Q. Strain engineering in perovskite solar cells and its impacts on carrier dynamics. *Nat. Commun.* **2019**, *10*, 815.
(40) Meng, L.; Sun, C.; Wang, R.; Huang, W.; Zhao, Z.; Sun, P.; Huang, T.; Xue, J.; Lee, J. W.; Zhu, C.; Huang, Y.; Li, Y.; Yang, Y. Tailored Phase Conversion under Conjugated Polymer Enables Thermally Stable Perovskite Solar Cells with Efficiency Exceeding 21. *J. Am. Chem. Soc.* **2018**, *140*, 17255−17262.
(41) Yang, Y. M.; Chen, X.; Liu, S.; Zhu, H.; Wang, W.; Kuang, C.; Liu, X. Characterizations and Understanding of Additives Induced Passivation Effects in Narrow-Bandgap Sn−Pb Alloyed Perovskite Solar Cells. *J. Phys. Chem. C* **2021**, *125*, 12560−12567.
(42) Pascual, J.; Flatken, M.; Felix, R.; Li, G.; Turren-Cruz, S. H.; Aldamasy, M. H.; Hartmann, C.; Li, M.; Di Girolamo, D.; Nasti, G.; Husam, E.; Wilks, R. G.; Dallmann, A.; Bar, M.; Hoell, A.; Abate, A. Fluoride Chemistry in Tin Halide Perovskites. *Angew. Chem., Int. Ed. Engl.* **2021**, *60*, 21583−21591.
(43) Chen, Q.; Luo, J.; He, R.; Lai, H.; Ren, S.; Jiang, Y.; Wan, Z.; Wang, W.; Hao, X.; Wang, Y.; Zhang, J.; Constantinou, I.; Wang, C.; Wu, L.; Fu, F.; Zhao, D. Unveiling Roles of Tin Fluoride Additives in High-Efficiency Low-Bandgap Mixed Tin-Lead Perovskite Solar Cells. *Adv. Energy Mater.* **2021**, *11*, 2101045.
(44) Chen, R.; Wang, Y.; Nie, S.; Shen, H.; Hui, Y.; Peng, J.; Wu, B.; Yin, J.; Li, J.; Zheng, N. Sulfonate-Assisted Surface Iodide Management for High-Performance Perovskite Solar Cells and Modules. *J. Am. Chem. Soc.* **2021**, *143*, 10624−10632.
(45) Chen, S.; Dai, X.; Xu, S.; Jiao, H.; Zhao, L.; Huang, J. Stabilizing perovskite-substrate interfaces for high-performance perovskite modules. *Science* **2021**, *373*, 902−907.
(46) Lin, Y.-H.; Sakai, N.; Da, P.; Wu, J.; Sansom, H. C.; Ramadan, A. J.; Mahesh, S.; Liu, J.; Oliver, R. D. J.; Lim, J.; Aspitarte, L.; Sharma, K.; Madhu, P. K.; Morales-Vilches, A. B.; Nayak, P. K.; Bai, S.; Gao, F.; Grovenor, C. R. M.; Johnston, M. B.; Labram, J. G.; Durrant, J. R.; Ball, J. M.; Wenger, B.; Stannowski, B.; Snaith, H. J. A piperidinium salt stabilizes efficient metal-halide perovskite solar cells. *Science* **2020**, *369*, 96−102.
(47) Domanski, K.; Alharbi, E. A.; Hagfeldt, A.; Gratzel, M.; Tress, W. Systematic investigation of the impact of operation conditions on the degradation behaviour of perovskite solar cells. *Nat. Energy* **2018**, *3*, 61−67.